The near field of coaxial jets: a numerical study

Guillaume Balarac, Olivier Métais

The near field of coaxial jets: A numerical study

Guillaume Balarac[a] and Olivier Métais
Équipe MoST/LEGI, Boîte Postale 53, 38041 Grenoble Cedex 09, France

The near-field behavior of coaxial jets is studied through direct numerical simulation (DNS) with a particular focus on the influence of the inner shear layer steepness characterized by its momentum thickness θ_{01} thus mimicking the variation in the lip thickness of a real jet nozzle. We investigate the two distinct jet regimes $r_u > r_{uc}$ for which a recirculation bubble is present near the jet inlet and $r_u < r_{uc}$ without any recirculation bubble, r_u being the velocity ratio between the outer jet and inner jet velocities. It is shown that small values of θ_{01} lead to a fast transition to turbulence. The various mechanisms leading to this transition are investigated in detail: the three-dimensionality growth, the appearance of secondary vortices superimposed on the main ring vortices, and the subsequent longitudinal stretching of streamwise vortices. This stretching mechanism is shown to play a dominant role in the transition processes towards a fully developed turbulent state. For high enough values of r_u, a pinching of the jet is observed near the inlet and it is shown that this pinching phenomenon lasts on a shorter downstream distance for small values of θ_{01} due to a more efficient turbulent mixing. In the $r_u > r_{uc}$ case, variations of θ_{01} strongly affect the shape and the downstream extent of the recirculation bubble. The DNS allow to show the strong dependency of the inner and outer potential core lengths and of the critical value r_{uc} on the jet inlet velocity profile. We finally revisit the theoretical model originally proposed by Rehab, Villermaux, and Hopfinger ["Flow regimes of large-velocity-ratio coaxial jets," J. Fluid Mech. **345**, 357 (1997)] first aimed at the prediction of the variations of various jet characteristics as a function of r_u. The model is extended to determine the dependency of the jet characteristics with θ_{01}. A very good correspondence between the theoretical predictions and the numerical results is obtained.

I. INTRODUCTION

Coaxial jets are present in various industrial devices: they effectively constitute an efficient way of mixing species for combustion applications. They are also used in aeroacoustics: the noise produced by a single jet can indeed be reduced thanks to the addition of a surrounding coaxial stream (e.g., Williams, Ali, and Anderson[1]).

Coaxial jets are composed of an inner jet issued from a nozzle of diameter D_1 and an outer annular jet issued from an outer annulus of diameter $D_2 (D_2 > D_1)$. U_1 and U_2 designate the respective velocities of the inner and outer jets. One of the important parameters characterizing the coaxial jet dynamics is the ratio between the outer to the inner jet momentum flux, $M = \rho_2 U_2^2 / \rho_1 U_1^2$ where ρ_1 and ρ_2 are, respectively, the inner and outer density (see Favre-Marinet and Camano Schettini[2]). For constant density jets ($\rho_1 = \rho_2$), the momentum flux ratio reduces to the velocity ratio, $r_u = U_2 / U_1$.

In the present study, we consider constant density coaxial jets for which the outer velocity is larger than the inner one ($r_u > 1$). These jets are situated in-between two limiting cases: a single round jet ($r_u = 1$) and a purely annular jet ($r_u \to \infty$). Purely annular jets are characterized by the presence of a big recirculation bubble near the jet axis (Ko and Chan[3]). This backflow region was experimentally observed by Rehab[4] and numerically by da Silva, Balarac, and Métais[5] for $r_u \gg 1$. Since this backflow is absent for small enough values of r_u, there exists a critical velocity ratio r_{uc} which separates the two different main flow regimes, without recirculation bubble for $1 < r_u < r_{uc}$ and with recirculation bubble for $r_u > r_{uc}$.

Rehab, Villermaux, and Hopfinger[6] experimentally showed that the coaxial jet dynamics and its vortex topology are strongly dependent on the shape of the inlet nozzle. Indeed, different shapes lead to significant variations of the two shear layers which are present in the coaxial jet: the inner shear layer at the interface between the inner and the outer jets and the outer shear layer on the external border of the outer jet. In the following, we will characterize the respective thicknesses of the inner and outer shear layers by their momentum thicknesses θ_{01} and θ_{02}. The previous experimental works[6] have mainly focused on the influence of r_u considering very small values of θ_{01} and θ_{02}. However, even for high Reynolds number jets, a variation of the inner lip thickness of the jet yields a significant variation of θ_{01}. The present paper completes the previous experimental and numerical works on coaxial jets by investigating the influence of θ_{01} on the transitional processes in the jet near field. We also vary the ratio r_u and the two distinct jet regimes are successively considered: the case without recirculation bubble ($r_u < r_{uc}$) and with recirculation bubble ($r_u > r_{uc}$). In particular, we will show that the value of r_{uc} varies widely with θ_{01}. This completes Rehab, Villermaux, and Hopfinger[7] observations

[a]Electronic mail: guillaume.balarac@hmg.inpg.fr

showing a strong dependence of r_{uc} with the jet nozzle shape with values located between 7 and 9.

As far as numerical investigations of coaxial jets are concerned, da Silva, Balarac, and Métais[5] (referred to as SBM) previously performed direct numerical simulations (DNS) of spatially growing coaxial jets for two values of r_u: r_u=3.3 and r_u=23.5. The ratio of the jet radius to the initial momentum thicknesses was fixed with R_1/θ_{01}=13 and $\theta_{01}=\theta_{02}$. In the present study, we widely vary the values of θ_{01}/R_1 and r_u. We furthermore develop simple theoretical models inspired by the ones originally proposed by Rehab, Villermaux, and Hopfinger[6] allowing to predict the variation laws of various statistical quantities in function of θ_{01}/R_1 and r_u.

In Sec. II, the numerical method, physical, and computational parameters of the DNS are detailed. Section III investigates how θ_{01} influences the near-field jet dynamics and the mechanisms of transition towards a fully developed turbulent state. The two flow regimes $r_u<r_{uc}$ and $r_u>r_{uc}$ are successively considered. Section IV extends the theoretical model originally proposed by Rehab, Villermaux, and Hopfinger[6] to predict the variation laws of various jet statistics as a function of θ_{01} and r_u.

II. NUMERICAL METHOD AND COMPUTATIONAL PARAMETERS

All the simulations presented here were performed with the same numerical code as the one used by SBM. The full three-dimensional incompressible Navier–Stokes equations, assuming constant density, are solved with a very precise numerical technique combining sixth-order "compact" (Lele[8]) scheme in the flow direction and pseudospectral (Canuto *et al.*[9]) schemes in the two-transverse directions. This code was originally developed by Gonze[10] and has been intensively validated both for round jets and plane jets configurations (see da Silva and Métais,[11] da Silva and Métais[12]). The detailed discretization procedure is described by Gonze[10] and by da Silva[13].

The velocity vector is decomposed as $\vec{U}=(u_x,u_y,u_z)$, where u_x designates the streamwise component, u_y and u_z are the two-transverse components. We also use a cylindrical coordinate system (x,r,θ) with x the streamwise (longitudinal) distance along the jet axis, r the distance from the jet axis, and θ the azimuthal angle. Any vector $\vec{a}$ will be decomposed, in this system, as $\vec{a}=(a_x,a_r,a_\theta)$ For all the simulated cases, the inlet velocity profile is given by

$$\vec{U}(\vec{x}_0,t)=\vec{U}_{\text{med}}(r)+\vec{U}_{\text{noise}}(\vec{x}_0,t), \tag{1}$$

where $\vec{U}(\vec{x}_0,t)$ is the instantaneous inlet velocity vector, which is prescribed at each time step. The inlet velocity profile $\vec{U}_{\text{med}}(r)$ mimics a realistic experimental profile: it is constructed with two hyperbolic tangent velocity profiles as shown in Fig. 1. It consists in a one-dimensional flow orientated along the x direction whose modulus is given by

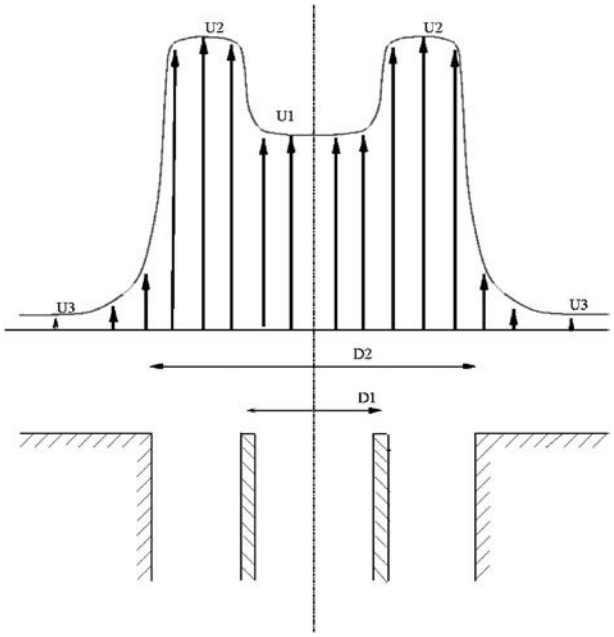

FIG. 1. Sketch of the inlet velocity profile. θ_{01} and θ_{02} are the momentum thicknesses for the inner shear layer (velocity jump from U_1 to U_2) and for the outer shear layer (velocity jump from U_2 to U_3), respectively.

$$U_{\text{med}}(r)=\begin{cases}\frac{U_1+U_2}{2}+\frac{U_1-U_2}{2}\tanh\left(\frac{r-R_1}{2\theta_{01}}\right) & \text{for } r<R_m\\ \frac{U_2+U_3}{2}+\frac{U_2-U_3}{2}\tanh\left(\frac{r-R_2}{2\theta_{02}}\right) & \text{for } r>R_m,\end{cases} \tag{2}$$

where U_1 is the inner coaxial jet velocity, U_2 is the outer velocity, and U_3 is a very small coflow. R_1, R_2, and $R_m=(R_1+R_2)/2$ are the inner, outer, and averaged radii, and θ_{01} and θ_{02} are the inlet momentum thicknesses from the inner and outer shear layers, respectively. For each station x, the inner and outer momentum thicknesses are defined by (3) and (4),

$$\theta_1(x)=\int_0^{R_m}\left[\frac{U_x(x,r)-U_{\min}(x)}{U_{\max}(x)-U_{\min}(x)}\right]\times\left[1-\frac{U_x(x,r)-U_{\min}(x)}{U_{\max}(x)-U_{\min}(x)}\right]dr, \tag{3}$$

$$\theta_2(x)=\int_{R_m}^{\infty}\left[\frac{U_x(x,r)-U_{\min}(x)}{U_{\max}(x)-U_{\min}(x)}\right]\times\left[1-\frac{U_x(x,r)-U_{\min}(x)}{U_{\max}(x)-U_{\min}(x)}\right]dr, \tag{4}$$

where $U_{\max}(x)$ and $U_{\min}(x)$ are, respectively, the maximum and minimum mean streamwise velocities for the inner or outer streams and $U_x(x,r)$ is the local mean streamwise velocity. The mean normal and spanwise velocities are set to zero at the inlet

$$V_{\text{med}}(\vec{x}_0)=W_{\text{med}}(\vec{x}_0)=0. \tag{5}$$

Note that the mean values are obtained through a temporal averaging based on a time interval long enough to reach statistical convergence. In the following, $\langle f\rangle(x,r)$ designates

the mean value of any quantity $f(x,r,\theta,t)$: $\langle f\rangle$ is independent of the azimuthal angle θ due to the axisymmetry of the flow configuration.

$\vec{U}_{\text{noise}}(\vec{x}_0,t)$ is the noise superimposed on the inlet profile. It is given by

$$\vec{U}_{\text{noise}}(\vec{x}_0,t) = A_n U_{\text{base}}(\vec{x}_0)\vec{f}'. \tag{6}$$

A_n is the maximum amplitude of the incoming noise and $U_{\text{base}}(\vec{x}_0)$ is a function that mainly locates the noise in the shear layer gradients:

$$U_{\text{base}}(\vec{x}_0) = \begin{cases} 0.5 & \text{if } 0.85 > r/R_1 \\ 1.0 & \text{if } 0.85 < r/R_1 < 1.15 \\ 1.0 & \text{if } 0.85 < r/R_2 < 1.15 \\ 0 & \text{otherwise,} \end{cases}$$

$\vec{f}'$ is a random noise designed to satisfy a given energy spectrum (see SBM for details). The random noise is applied on the three velocity components.

All simulations are carried out on the same computational grid consisting in $231\times384\times384$ points for a domain size of $10.8D_1\times10.65D_1\times10.65D_1$, along the streamwise ($x$) and the two transverse directions (y,z), the mesh size being uniform in all three directions. In all simulations, the Reynolds number and the ratio of the outer to the inner diameter are $\text{Re}_{D_1}=U_2D_1/\nu=3000$ and $D_2/D_1=2$, respectively. The ratio of the jet outer radius to the outer initial shear layer momentum thickness is fixed with $R_2/\theta_{02}=25$. The maximum noise amplitude is set to $A_n=3.0\%$. A very small coflow is imposed such that $U_3/U_2=0.04$: it was shown not to influence the jet dynamics (see da Silva[13]).

As previously pointed out, the goal of the present study is mainly to look at the influence of the parameter θ_{01}. r_u is also varied to investigate the two flow regimes, with and without recirculation bubble. Table I synthesizes the various runs which were carried out: θ_{01}/R_1 varies from 0.04 to 0.1 and r_u widely ranges from 3 to 30. Note that each simulation series DNS*i* (with *i* varying from 1 to 5) corresponds with a fixed value of the parameter θ_{01}/R_1. For convenience, both parameters θ_{01}/R_1 and its opposite R_1/θ_{01} will be successively used.

It is important to note that the potential sources of numerical and modeling errors have been minimized in the present study. Indeed, precise numerical methods, a well-resolved regular mesh and direct numerical simulations are used. The price to pay is that the Reynolds number for our simulations ($\text{Re}_{D_1}=3000$) is lower than the values usually encountered in the experimental studies (see, i.e., Rehab *et al.*,[6] Warda, Kassab, Elshorbagy, and Elsaadawy,[14] Buresti, Petagna, and Talamelli[15]). Furthermore, to properly discretize the velocity gradient, relatively large values of θ_{01} and θ_{02} have to be considered. The values usually considered in previous experiments are usually much smaller: this renders any validation by comparison with experimental data difficult. Previous experimental studies (Ko and Kwan[16] and Ko and Chan[3]) have however shown that in the far field of coaxial jets a self-similar state is reached similar to the one reached in a single jet. SBM recovered this result with the present numerical code (see their Fig. 7). We here complete this previous validation by considering the near-field behavior in the vicinity of the jet inlet. Figure 2 displays the downstream evolution of the rms velocity component $\langle u'^{2}_{x}\rangle^{1/2}(x,r)$ at the jet centerline for the two simulations DNS4_3 ($r_u=3$; $R_1/\theta_{01}=20$) and DNS5_17 ($r_u=17$; $R_1/\theta_{01}=25$). Note that the first simulation corresponds with the case with no recirculation bubble while a bubble is present in the second simulation. The numerical results are compared with two different experiments: the first by Buresti *et al.*[15] corresponding to $r_u=3$, $\text{Re}_{D_1}\approx160\,000$, $R_1/\theta_{01}\approx70$, and $R_2/\theta_{02}\approx130$, the second by Rehab *et al.*[6] ($r_u=9$, $\text{Re}_{D_1}\approx200\,000$, $R_1/\theta_{01}\approx100$, and $R_2/\theta_{02}\approx100$). In the first experiment, $r_u<r_{uc}$ while $r_u>r_{uc}$ in the second. Despite the difference in the Reynolds numbers and the steepness of the velocity gradients a good agreement is observed between the numerical and experimental data. Note that a virtual origin x_0, with $x_0\approx1D_1$ has been used for the two DNS to account for the Reynolds number difference with the experimental value: indeed, the turbulence develops at much shorter downstream distance in a high Reynolds number jet.

TABLE I. Description of the various runs.

Category	Name	r_u	R_1/θ_{01}	θ_{01}/R_1
	DNS1_3	3	10	0.1
DNS1	DNS1_10	10	10	0.1
	DNS1_17	17	10	0.1
	DNS2_3	3	12.5	0.08
	DNS2_5	5	12.5	0.08
	DNS2_6	6	12.5	0.08
DNS2	DNS2_7	7	12.5	0.08
	DNS2_10	10	12.5	0.08
	DNS2_13	13	12.5	0.08
	DNS2_17	17	12.5	0.08
	DNS2_30	30	12.5	0.08
	DNS3_11	11	15	0.0667
DNS3	DNS3_13	13	15	0.0667
	DNS4_3	3	20	0.05
	DNS4_10	10	20	0.05
DNS4	DNS4_12	12	20	0.05
	DNS4_17	17	20	0.05
	DNS5_10	10	25	0.04
DNS5	DNS5_11	11	25	0.04
	DNS5_17	17	25	0.04

III. INFLUENCE OF THE INNER SHEAR LAYER THICKNESS ON THE JET DYNAMICS

A. Coaxial jet without recirculation bubble $r_u<r_{uc}$

1. Mechanisms leading to turbulent transition

We first consider the case where no recirculation bubble is present. The influence of the shear layer thickness θ_{01} is investigated by first focusing on the comparison of the three simulations DNS1_10 ($r_u=10$; $\theta_{01}/R_1=0.1$), DNS2_10 (r_u

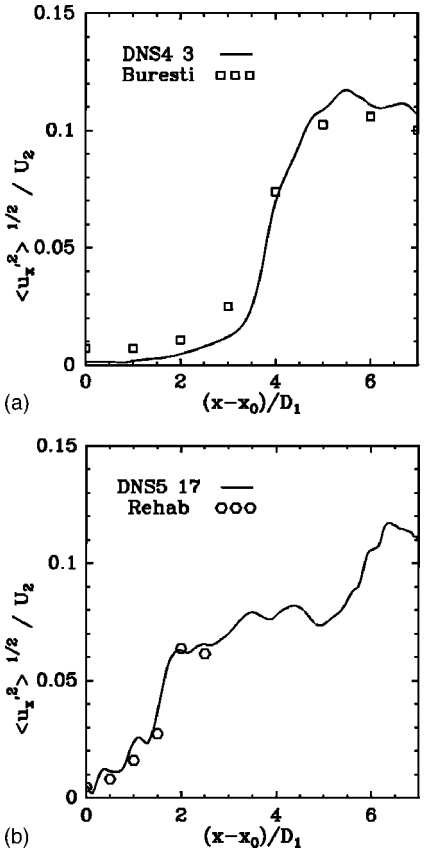

FIG. 2. Downstream evolution of the axial velocity component rms $\langle u'^{2}_{x}\rangle^{1/2}(x,r=0)$ at the jet centerline: (a) DNS4_3 and (b) DNS5_17. The numerical results are compared with the measurements by Buresti *et al.* (Ref. 15) and Rehab *et al.* (Ref. 6).

$=10$; $\theta_{01}/R_1=0.08$), and DNS5_10 ($r_u=10$; $\theta_{01}/R_1=0.04$). To characterize, the transition from a quasilaminar regime near the inlet to a fully developed turbulent regime we first consider the downstream evolution of $\langle u'^{2}_{x}\rangle^{1/2}(x,r)$ (Fig. 3). r is here taken equal to R_1 corresponding to the radial location of the vorticity local maximum within the inner shear layer of the inlet profile. For the three considered cases, the

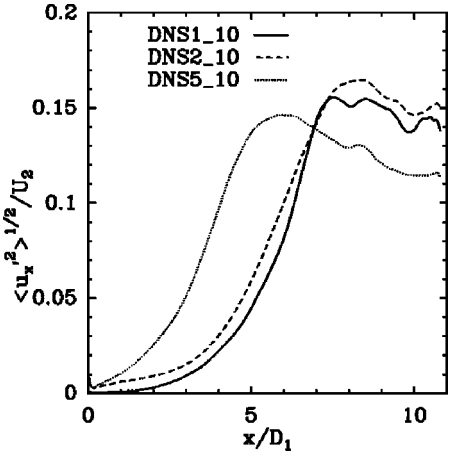

FIG. 3. Downstream evolution of the axial velocity component rms $\langle u'^{2}_{x}\rangle^{1/2}(x,r=R_1)$ at the inner shear layer for the three simulations (DNS1_10, DNS2_10, and DNS5_10).

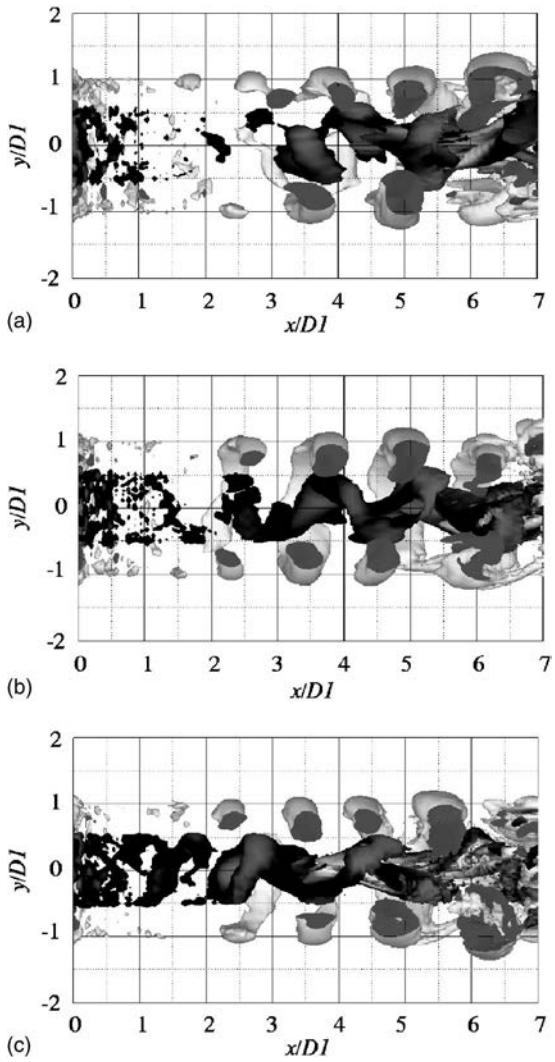

FIG. 4. Visualization of the coherent structures for the three simulations DNS1_10 (a), DNS2_10 (b), and DNS5_10 (c). Cut view of isosurfaces of positive $Q=0.5(U_2/D_1)^2$ colored by the azimuthal vorticity. Light gray corresponds with negative values and dark gray with positive values.

turbulence first undergoes a slow downstream growth before exhibiting a sudden transition characterized by a much faster growth. The transition location is situated further and further downstream as θ_{01} increases: it is indeed located around $x/D_1\approx 5$ for DNS1_10, $x/D_1\approx 4$ for DNS2_10, and $x/D_1\approx 2$ for DNS5_10. This faster transition can be explained by the fact that the instability of the inner shear layer leads to the generation of smaller scales for smaller values of θ_{01} and the transition towards turbulence is consequently faster.

This is clearly illustrated by Fig. 4 which shows isosurfaces of positive Q for the three simulations DNS1_10, DNS2_10, and DNS5_10. We recall that Q is the second invariant of the velocity gradient tensor defined as

$$Q=\tfrac{1}{2}(\Omega_{ij}\Omega_{ij}-S_{ij}S_{ij}), \tag{7}$$

where Ω_{ij} and S_{ij} are the antisymmetrical and symmetrical part of the velocity gradient tensor, respectively. The positive Q criterion was first proposed by Hunt, Wray, and Moin[17] and is now well recognized as a good way to identify the flow coherent vortices (see, e.g., Dubief and Delcayre[18]). In

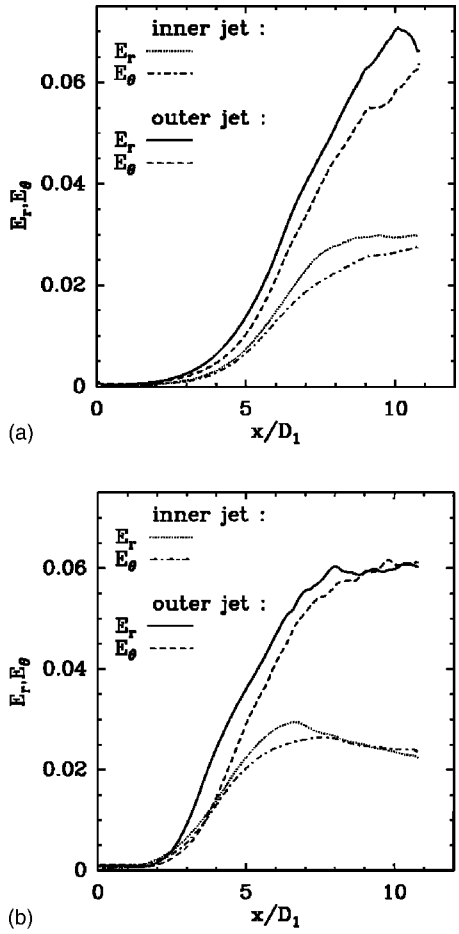

FIG. 5. Downstream evolution of radial and azimuthal contributions for the turbulent kinetic energy E_r and E_θ [see Eqs. (8)–(11) for definition] calculated in the inner and outer shear layer for the two simulations: (a) DNS2_10 and (b) DNS5_10.

particular, it can been showed that the positive Q regions are in good correspondence with low-pressure regions and thus constitute good tracors of intense vortices (see Métais[19]). Figure 4 shows the coherent structures development near the jet inlet ($0<x/D_1<7$). As pointed out by SBM, we assist in the shedding of both outer and inner vortices, respectively, associated with the instability of the outer and inner shear layers. For $r_u<r_{uc}$, the outer vortices impose their shedding frequency to the inner vortices and the latter are trapped between two consecutive larger vortex rings.[20] As previously pointed out, the instability develops faster when θ_{01} is decreased and the inner layer vortices are shed at shorter and shorter locations when we go from DNS1_10 to DNS5_10 simulation. Although the value of θ_{02} is identical in the three simulations, it is interesting to note that the outer vortices are also shed at shorter downstream distances for the smaller values of θ_{01}. This is attributable to the mutual interaction between the inner and outer shear layers: the faster growth of the disturbance within the inner shear layer induces an earlier destabilization of the outer layer. Since the DNS5_10 case is associated with an early development of the vortices, these are more rapidly subject to a three-dimensionalization process. It is clearly illustrated on Fig. 5 which shows the downstream evolution of E_r and E_θ for the inner shear layer and the outer shear layer. Only the two runs DNS2_10 and DNS5_10 are compared here. These quantities are the contributions of the radial (E_r) and azimuthal (E_θ) Reynolds stresses to the turbulent kinetic energy at a given x location (see SBM). They are defined as

$$E_r(x) = \sqrt{\frac{2\pi}{L_y L_z}\int_0^{R_m} \langle u_r'^2\rangle(x,r) r\, dr}, \tag{8}$$

$$E_\theta(x) = \sqrt{\frac{2\pi}{L_y L_z}\int_0^{R_m} \langle u_\theta'^2\rangle(x,r) r\, dr} \tag{9}$$

for the inner shear layer and as

$$E_r(x) = \sqrt{\frac{2\pi}{L_y L_z}\int_{R_m}^{\infty} \langle u_r'^2\rangle(x,r) r\, dr}, \tag{10}$$

$$E_\theta(x) = \sqrt{\frac{2\pi}{L_y L_z}\int_{R_m}^{\infty} \langle u_\theta'^2\rangle(x,r) r\, dr} \tag{11}$$

for the outer shear layer. u_r' and u_θ' are, respectively, the radial and azimuthal components of the fluctuating velocity field. Note that, for a purely axisymmetric vortex ring with no swirl, the component E_θ would be identically zero. E_θ then represents the departure from axisymmetry and therefore constitutes a measure of the three-dimensionality level. For both DNS2_10 and DNS5_10 cases, E_r, associated with the growth of the vortex rings, dominates E_θ during the first stage of the transition: this indicates a weak degree of three-dimensionalization in this early stage. Further downstream, E_θ catches up with E_r showing a full three-dimensionalization of the jet (see da Silva and Métais[11]). The comparison of Figs. 5(a) and 5(b) clearly indicates that the three-dimensionalization processes become dominant on a shorter downstream distance for the DNS5_10 simulation than for the DNS2_10 simulation. A fully developed turbulent state is reached at $x/D_1 \approx 8$ for DNS5_10 when the computational box is too short for such a state to be observed for DNS2_10.

It is clear from Fig. 4 that the three-dimensionalization process is strongly linked with the appearance of streamwise secondary vortices. These appear much sooner when θ_{01} is smaller and induce a strong three-dimensionalization of the inner and outer vortices between which they are stretched and consequently trigger an earlier transition towards a fully turbulent regime. Figures 6(a) and 6(b) display a zoom of the three-dimensional coherent structures in the transition region situated between $x/D_1=3$ and $x/D_1=7$ for DNS5_10 simulation. The secondary streamwise vortices appear and are stretched both between two consecutive inner vortices [Fig. 6(a)] and between two consecutive outer vortices [Fig. 6(b)]. Note that, for DNS5_10 simulation, the inner streamwise vortices form at a shorter downstream distance than the outer vortices which appear further downstream. This difference in behavior between the inner and outer shear layer is explained below.

The strong amplification of the streamwise vorticity as one moves downstream is illustrated in Fig. 7 which shows the profile of $\langle \omega_x'^2\rangle(x,r)$ as a function of r for several down-

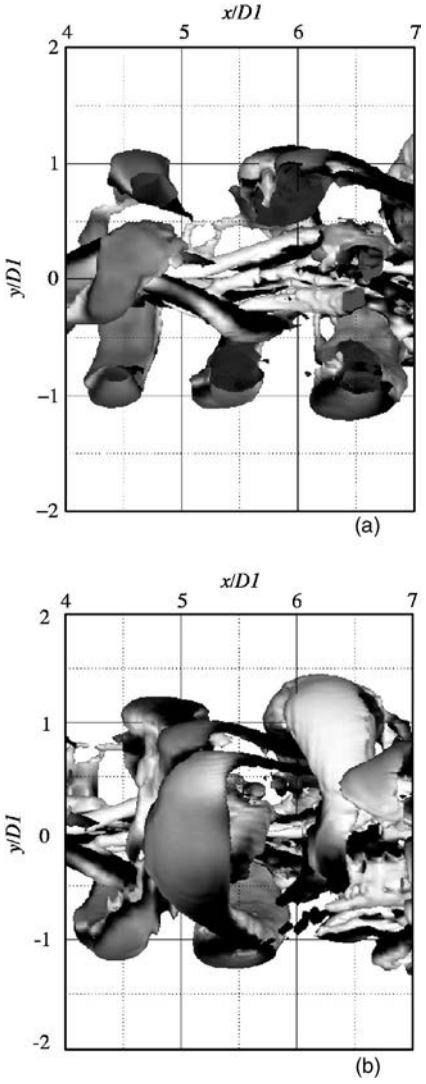

FIG. 6. Zoom showing the secondary streamwise vortices in simulation DNS5_10: (a) vortices stretched between two consecutive inner vortices (cut view); (b) vortices stretched between two consecutive outer vortices. Isosurfaces of positive $Q=0.5(U_2/D_1)^2$ colored by the axial vorticity. Light gray corresponds with negative values and dark gray with positive values.

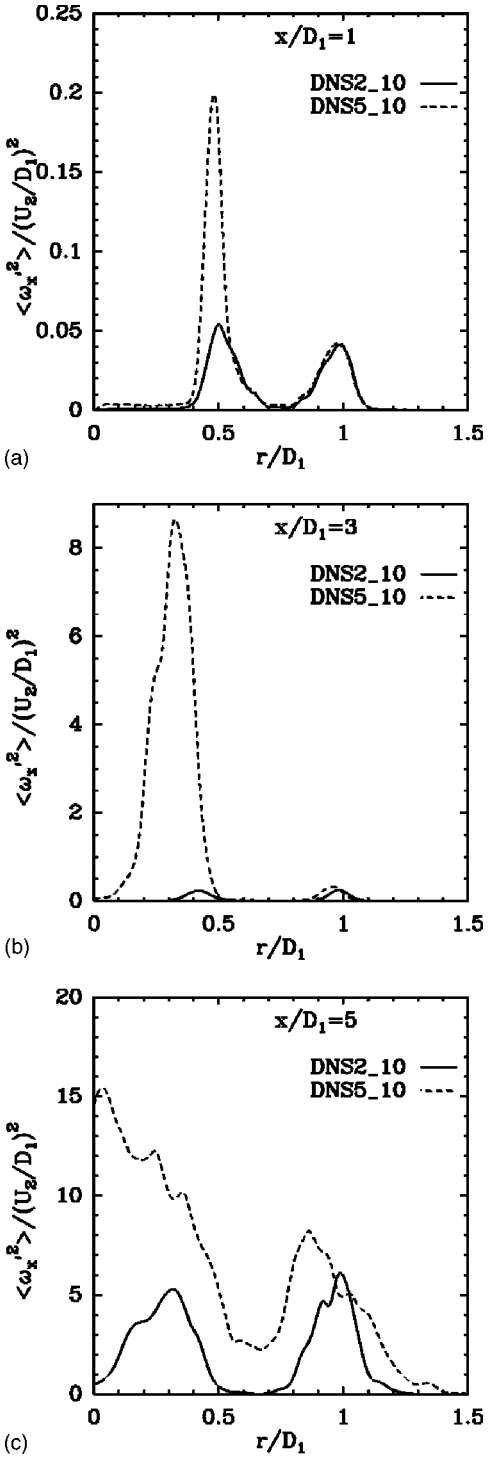

FIG. 7. Radial profile of $\langle \omega'^{2}_{x} \rangle(x,r)$ at three downstream location (x/D_1 =1, 3, and 5) for the two simulations (DNS2_10 and DNS5_10).

stream locations $x/D_1=1$, 3, and 5. The two simulations DNS2_10 and DNS5_10 are here compared. DNS2_10 corresponds with a case where the momentum thicknesses of the inner and outer shear layers are identical ($\theta_{01}=\theta_{02}$). The growth of the three dimensionality takes place at a similar rate within both shear layers: this gives rise to two longitudinal vorticity peaks of comparable intensity, respectively, situated at $r/D_1\approx 0.5$ and $r/D_1\approx 1$. The longitudinal vorticity stretching between the main jet vortices, previously mentioned, yields a significant increase of the vorticity peak amplitude as we move downstream. Conversely, DNS5_10 corresponds to a case where the two momentum thicknesses differ: here $\theta_{01}=\theta_{02}/2$. In that case, the streamwise vortices are first stretched between two consecutive vortices of the inner layer yielding a strong amplification for $r/D_1\leqslant 0.5$ (see Fig. 7 at $x/D_1=3$). The stretching between two consecutive outer vortices takes place only further downstream leading to a later longitudinal vorticity enhancement in the outer shear layer region near $r/D_1\approx 1$ (Fig. 7 at $x/D_1=5$).

Figure 8 compares the profiles of the three rms vorticity components $\langle \omega'^{2}_{x} \rangle(x,r)$, $\langle \omega'^{2}_{r} \rangle(x,r)$, and $\langle \omega'^{2}_{\theta} \rangle(x,r)$ for the two simulations DNS2_10 ($x/D_1=6$) and DNS5_10 ($x/D_1=3$). This figure confirms that longitudinal stretching is the dominant factor leading to transition to a fully developed turbulent regime: indeed, the longitudinal vorticity component clearly dominates the other two components. We have

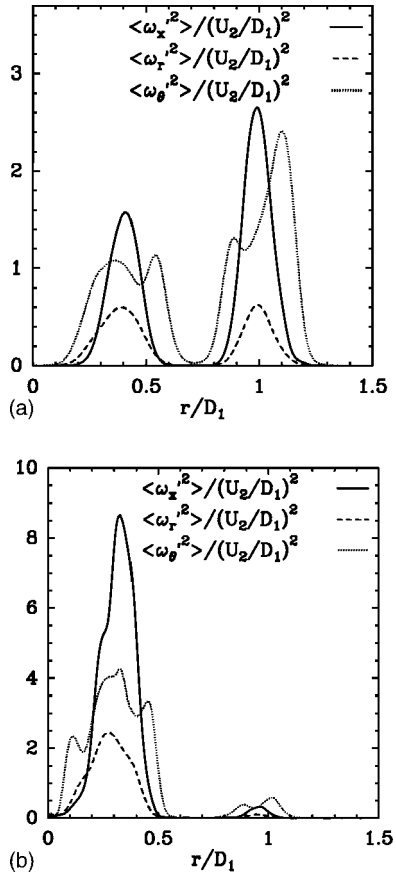

FIG. 8. Comparison between $\langle \omega'^2_x \rangle(x,r)$, $\langle \omega'^2_r \rangle(x,r)$, and $\langle \omega'^2_\theta \rangle(x,r)$ profiles: (a) simulation DNS2_10 at the location $x/D_1=6$; (b) simulation DNS5_10 at $x/D_1=3$.

checked that the ratio between the peak values of ω'_x and ω'_r reaches a maximum of 4.5 for DNS2_10 and 5 for DNS5_10 as we move downstream: this maximum being respectively reached at $x/D_1=4.5$ (DNS2_10) and at $x/D_1=2.5$ (DNS5_10). Similarly, the corresponding maximal ratio between ω'_x and ω'_θ are, respectively, 1.5 for DNS2_10 and 2 for DNS5_10 and take place at $x/D_1=6$ and $x/D_1=3.5$.

2. Jet spreading and potential cores

We now investigate the influence of θ_{01} on more global quantities. We first consider the jet spreading rate defined through a global shear layer thickness by analogy with the definition used for single jets. Let $r_{\max}(x)$ be the radial distance for which the mean streamwise velocity reaches its maximum value, $\max[U_x(x,r)]=U_x(x,r_{\max}(x))$. $\delta(x)$ is then chosen as the radial distance such that

$$U_x(x,\delta(x)) = \tfrac{1}{2}[U_x(x,r_{\max}(x)) - U_3], \tag{12}$$

where U_3 is the streamwise velocity in the irrotational region. Since we are interested in the global spreading rate of the jet, we furthermore choose $\delta(x)$ such that $\delta(x) > r_{\max}(x)$: $\delta(x)$ therefore characterizes the jet width. The downstream evolution of $\delta(x)$ for the three simulations DNS1_10, DNS2_10, and DNS5_10 is shown in Fig. 9. The simulation DNS2_3 corresponding to a smaller value of r_u ($r_u=3$; $\theta_{01}/R_1=0.08$) is also shown for comparison. For

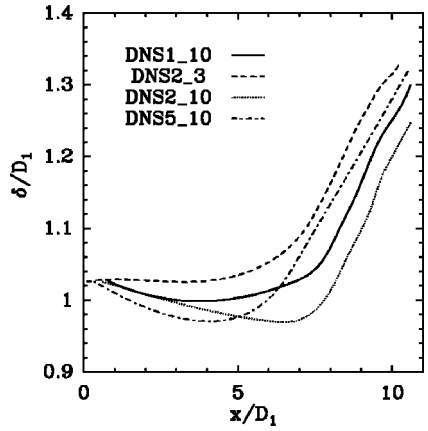

FIG. 9. Downstream evolution of jet spreading rate for the four simulations DNS1_10, DNS2_3, DNS2_10, and DNS5_10.

the simulation with moderate r_u (DNS2_3), $\delta(x)$ behaves similarly to a single jet: it is indeed almost constant for $x/D_1<7$ and undergoes a sudden transition with a rapid growth for $x/D_1>7$. In this second stage, transition to turbulence has taken place and the linear growth characteristic of the turbulent regime is observed. We have checked that the slope in the linear regime closely coincides with the slope for a single jet. For the cases with larger r_u (DNS1_10, DNS2_10, and DNS5_10), a decrease of δ is observed before transition. This corresponds to a so-called pinching phenomenum of the coaxial jet which has previously been observed experimentally.[4] For large enough values of r_u, the velocity difference between the outer jet and the inner jet induces a curvature of the outer mean streamlines towards the jet axis. This is directly related to the fluid entrainment by the outer coaxial jet: a limited amount of fluid can indeed be entrained from the slow part of the jet core and this entrainment eventually leads to a fluid depletion in the core region. This fluid depletion is accompanied by a pressure drop within the jet core leading to a curvature of the streamlines towards the jet axis. As previously mentioned, for r_u larger than the critical value r_{uc} it eventually yields a reverse backflow near the jet axis.

The comparison of DNS1_10, DNS2_10, and DNS5_10 allows to show that the pinching phenomenon is also strongly influenced by the value of the momentum thickness θ_{01}. For a fixed value of r_u, the decrease of θ_{01} is indeed associated with a decrease of the inner jet bulk velocity. One can then anticipate that the fluid depletion leading to a low-pressure region within the jet core will be more pronounced for small values of θ_{01} since a smaller quantity of fluid is injected within the core by the inner jet. This is confirmed by Fig. 9 which shows that the initial decrease of δ is more and more pronounced as we go from DNS1_10 to DNS5_10. The transition towards a turbulent linear growth occurs however at a shorter downstream location when θ_{01} is small. This is due to a faster transition to turbulence in that case as shown in Fig. 3. It is important to remark that the linear growth rate in the turbulent regime is identical for all the considered cases and becomes independent of the initial transitional stage. Note that the comparison of Figs. 3 and 9 indicates

that the effect of the turbulence growth has a delayed effect on the spreading rate. Indeed, it was observed on Fig. 3 that the rapid growth of $\langle u'^2_x \rangle^{1/2}$ due to transition was taking place at $x/D_1 \approx 5$, $x/D_1 \approx 4$, and $x/D_1 \approx 2$ for DNS1_10, DNS2_10, and DNS5_10, respectively. As shown on Fig. 9, this turbulence amplification has a direct effect on the spreading rate only for $x/D_1 \geqslant 7$, $x/D_1 \geqslant 7$, and $x/D_1 \geqslant 5$ for DNS1_10, DNS2_10, and DNS5_10, respectively. This is attributable to the fact that the turbulence originates from the inner shear layer and requires some downstream distance to diffuse towards the jet exterior and efficiently affect the jet spreading rate.

We now investigate how the two potential cores of the jet are affected by a variation in the value of θ_{01}. For a single jet, the potential core is the region where the flow remains free from the influence of viscosity. In this cone shaped region the flow is potential and conserves the streamwise velocity it had at the inlet. For the coaxial jet, we can define two potential cores, one for the inner round jet $0 < r < R_1$ and another for the outer annular flow $R_1 < r < R_2$. For these two inner and outer flow regions, the center of the respective potential cores can be identified as the radial locations at which the inlet streamwise velocity is conserved on the longest downstream distance. We call r_{PC1} and r_{PC2} these two radial locations for the inner and outer potential cores. Note that $r_{\mathrm{PC1}} = 0$. We define the length of the potential cores as the two longest distances we just defined: they are designated as $L_{\mathrm{PC}i}$ with $i = 1$ for the inner potential core and $i = 2$ for the outer one. From a practical point of view, $L_{\mathrm{PC}i}$ are determined as the two downstream distances from the inlet at which the mean streamwise velocity starts to differ by more than 5% from its value at the inlet.

The faster transition to turbulence associated with the decrease of θ_{01}, is clearly illustrated by Fig. 10 which shows the variations with R_1/θ_{01} of L_{PC1} and L_{PC2} at fixed r_u($r_u = 10$). The parameter R_1/θ_{01} is used here for a better readability of the figures: the simulations DNS1_10, DNS2_10, and DNS5_10 correspond to $R_1/\theta_{01} = 10$, 12.5, and 25. The increasingly efficient mixing of momentum due to turbulence when θ_{01} decreases yields a diminution of both L_{PC1} and L_{PC2}. Note that L_{PC1} varies with r_u (see below) while previous studies showed that L_{PC2} is independent of r_u (see Rehab, Villermaux, and Hopfinger[7]).

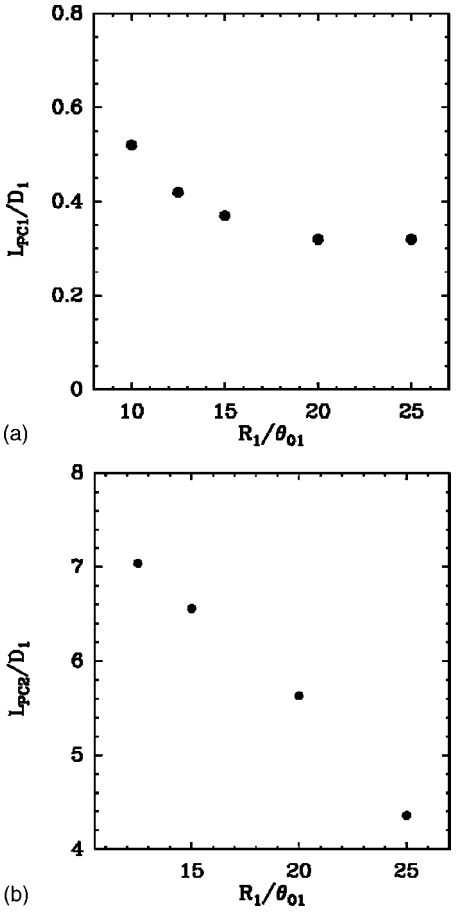

FIG. 10. (a) Evolution of the inner potential core length L_{PC1} with R_1/θ_{01} (at $r_u = 10$). (b) Evolution of the outer potential core length L_{PC2} with R_1/θ_{01} (at $r_u = 10$).

B. Recirculation bubble

We here consider the regime such that $r_u > r_{uc}$. To investigate the influence of θ_{01} two simulations are here compared DNS2_17 ($r_u = 17$; $\theta_{01}/R_1 = 0.08$) and DNS5_17 ($r_u = 17$; $\theta_{01}/R_1 = 0.04$). As r_u increases the entrainment by the outer annular jet and the depletion of the inner fluid is more and more pronounced. When r_u exceeds r_{uc}, the inner potential core breaks and a backflow region establishes associated with negative streamwise velocity near the jet axis. Figure 11 displays the downstream evolution of the mean axial velocity on the jet axis for the two simulations DNS2_17 and DNS5_17. In both cases, a region of negative velocity is apparent near the jet inlet. The longitudinal extent of the recirculation region varies with θ_{01} with a smaller value for sharper velocity gradients: the end of the recirculation bubble is located around $x/D_1 \approx 2.5$ for DNS5_17 when it ends around $x/D_1 \approx 3.5$ for DNS2_17.

The variation in size of the recirculation bubble is confirmed by Fig. 12 which shows positive Q isosurfaces for DNS2_17 and DNS5_17. In both cases, a recirculation bubble is seen to appear near the jet inlet but its longitudinal extension is significantly reduced for DNS5_17. Figure 13 displays a zoom on the recirculation bubble for both simulations. In both cases, the backflow region is centred at $x/D_1 \approx 2$ but the shape of the bubble significantly varies in function of θ_{01}: for DNS2_17 which corresponds to a relatively large value of θ_{01}, the Kelvin–Helmholtz vortices of the inner shear layer have not yet developed at this downstream location. Conversely, DNS5_17 corresponds with a value of θ_{01} which is twice smaller yielding an earlier formation of the Kelvin–Helmholtz vortices. In the first case, the bubble is then surrounded by a quasilaminar flow and it exhibits a very smooth shape. This is no longer the case in the second case where the recirculation bubble is significantly perturbed by the surrounding vortices of the inner shear layer. This has a significant impact on the flow turbulent behavior. Figure 14 indeed shows the downstream evolution of the rms velocity component $\langle u'^2_x \rangle^{1/2}(x,r)$ at the jet centerline for both simulations DNS2_17 and DNS5_17, this rms quantity being a

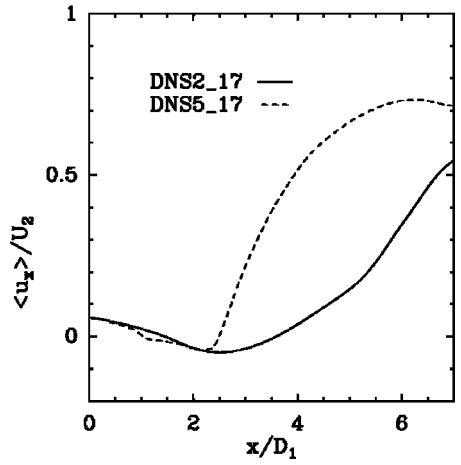

FIG. 11. Downstream evolution of the axial mean velocity at the centerline ($r=0$) for the two simulations DNS2_17 and DNS5_17.

measure of the turbulent activity in the backflow region ($1<x/D_1<4$). The recirculation bubble is seen to be laminar for DNS2_17 with $\langle u'^2_x\rangle^{1/2}\approx 0$ within the bubble. Conversely, the turbulent activity in the bubble is important for DNS5_17. Note that, in DNS2_17, a peak is present at $x/D_1\approx 0.75$ due to the turbulent production associated with the strong streamwise gradient of the mean streamwise velocity component corresponding to the flow deceleration in the stagnation region at the upstream part of the bubble (see SBM).

As already shown by SBM, Fig. 12 confirms that very elongated and intense longitudinal vortices form just downstream of the bubble. The downstream end of the recirculation bubble corresponds with an important longitudinal gradient of longitudinal velocity and consequently with a significant production of streamwise vorticity. This is confirmed by Figs. 15(a) and 15(b) which, respectively, represent the downstream evolution of the maximum value of the longitudinal vorticity rms $\langle\omega'^2_x\rangle$. The two simulations, DNS2_17 and DNS5_17, with a recirculation bubble are compared with the corresponding simulations without a recirculation bubble, DNS2_10 and DNS5_10. A strong increase of the longitudinal vorticity component in the flow region just downstream of the recirculation bubble is ob-

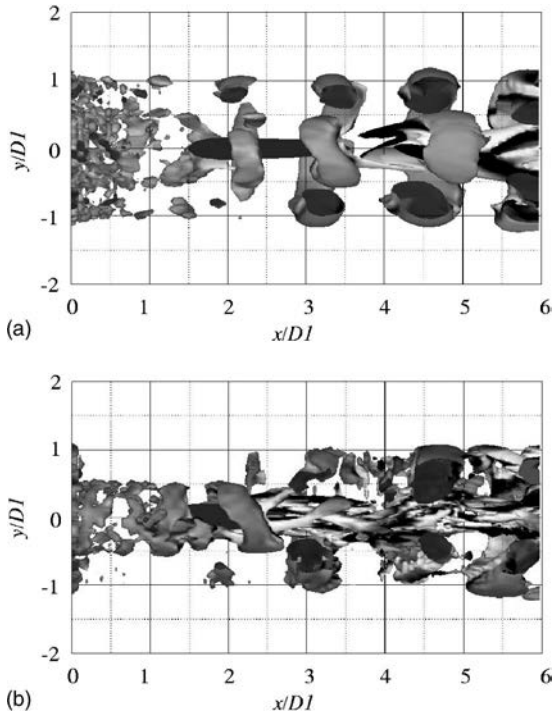

FIG. 12. Visualization of the coherent structures of DNS2_17 (a) and DNS5_17 (b) simulations near the jet inlet. Cut view of the isosurfaces of $Q=0.5(U_2/D_1)^2$ colored by the streamwise vorticity. Light gray corresponds with negative values and dark gray with positive values.

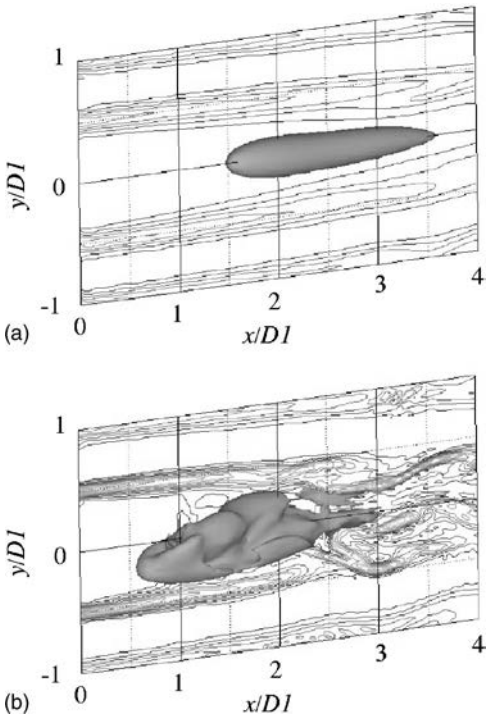

FIG. 13. Isosurface of zero velocity (light gray) showing the recirculation bubble and contours of vorticity modulus in the jet central plane: (a) DNS2_17 and (b) DNS5_17.

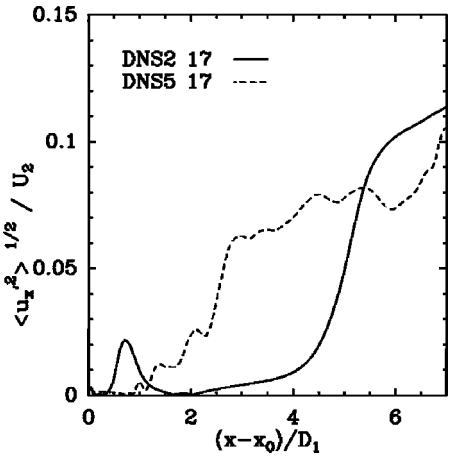

FIG. 14. Downstream evolution of the axial velocity component rms $\langle u'^2_x\rangle^{1/2}(x,r=0)$ at the jet centerline for the two simulations DNS2_17 and DNS5_17.

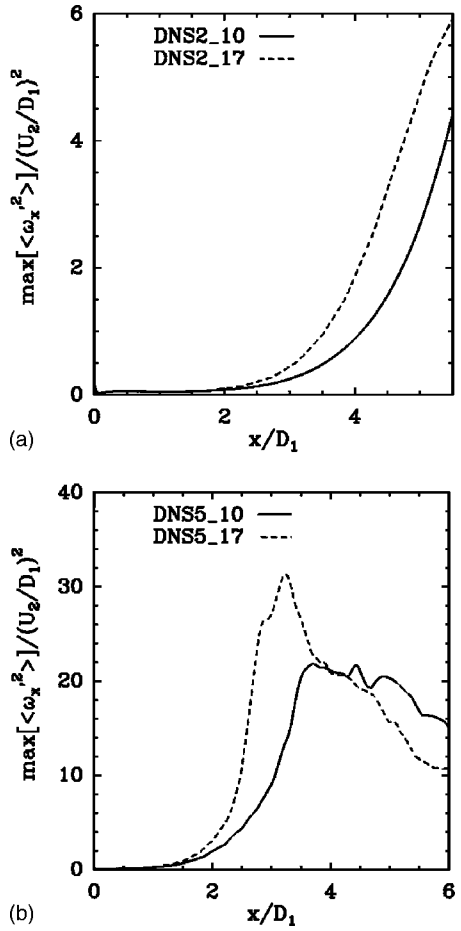

FIG. 15. Downstream evolution of the maximal value of $\langle \omega'^2_x \rangle$: (a) DNS2_10 and DNS5_17; (b) DNS5_10 and DNS5_17.

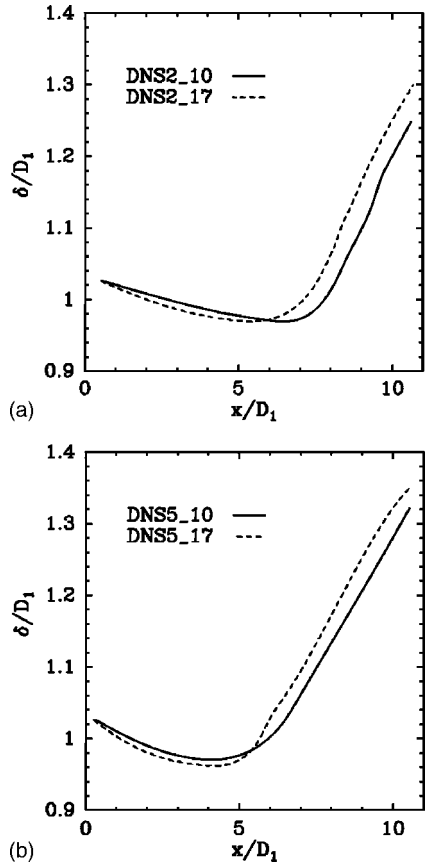

FIG. 16. Downstream evolution of the jet spreading rate δ: (a) DNS2_10 and DNS2_17; (b) DNS5_10 and DNS5_17.

served for both simulations DNS2_17 and DNS5_17. The peak value reached by this maximum is much larger than for the corresponding cases without a recirculation bubble: this indicates that the vortex stretching mechanisms are much more efficient in the presence of the bubble.

The streamwise vorticity generation just downstream the recirculation bubble triggers a fast transition towards a fully developed turbulent regime. This is illustrated by Figs. 16(a) and 16(b) which show the downstream evolution of the jet spreading rate $\delta(x)$ [see Eq. (12) for definition]: DNS2_17 and DNS5_17 are, respectively, compared with DNS2_10 and DNS5_10. The previously mentioned pinching phenomenum is observed in the two cases with the recirculation bubble and is even more pronounced than for the cases where the bubble is not present. However, for the two values of θ_{01} here considered, the enhanced turbulent activity downstream of the recirculation bubble leads to an earlier linear turbulent growth. It is important to note that the pinching phenomenum reaches a limiting value for the $r_u > r_{uc}$: indeed the minimum value reached by δ is almost identical for DNS2_17 and for DNS5_17. This is confirmed by Fig. 17 which shows the variation with r_u of the radial location of the outer potential core r_{PC2} (see preceding section). The DNS2 series of simulations are here considered corresponding to $R_1/\theta_{01}=12.5$. Due to the pinching phenomenum previously mentioned, the radial extension of the outer potential core is more and more reduced when r_u is increased. This is confirmed by the experimental observations of Rehab.[4] We remark that a plateau is reached when r_u exceeds the critical value r_{uc} for which a recirculation bubble appears (here $r_{uc}=13$), showing a limitation of the pinching phenomenum in the presence of a reverse flow region.

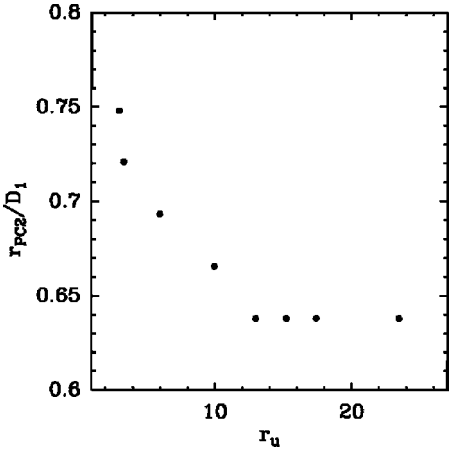

FIG. 17. Evolution with r_u of the radial localization r_{PC2} of the outer potential (at $R_1/\theta_{01}=12.5$).

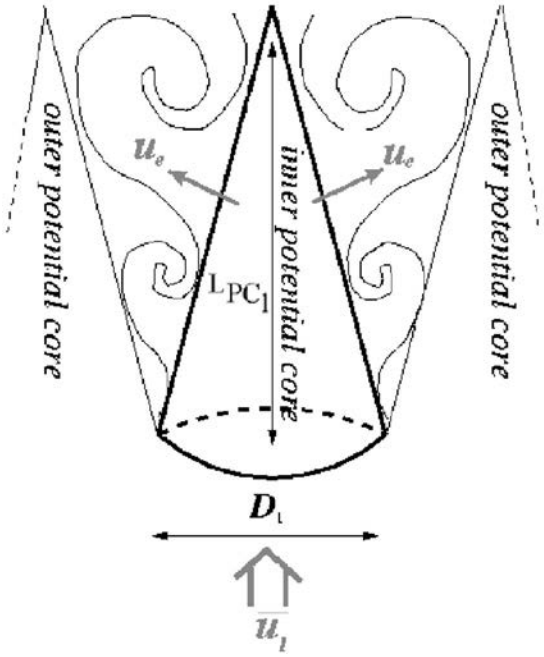

FIG. 18. Schematic diagram of the inner potential core: $\overline{u_1}$ designates the inner jet bulk velocity and u_e the entrainment velocity of the inner jet fluid into the mixing layer.

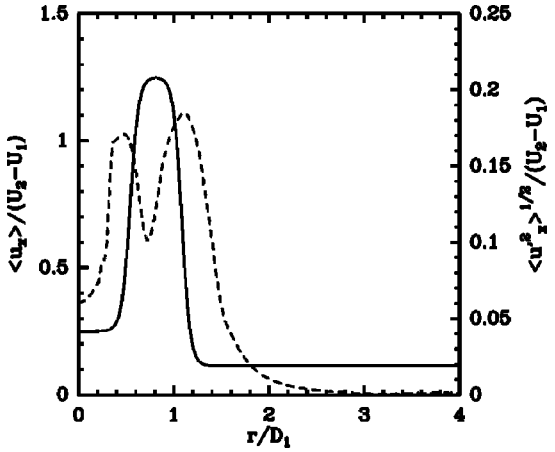

FIG. 19. Radial profiles of the mean axial velocity (continuous line) and of the rms of the longitudinal velocity fluctuation (dashed line) for DNS2_5 simulation. The profiles are computed at $x/D_1=1$.

IV. THEORETICAL MODELS

Rehab *et al.*[6] (referred to as RVH) proposed a theoretical model aimed at the prediction of the variation with r_u of the inner potential core length L_{PC1}. Since for their experimental setup, the inner jet profile was very steep with $R_1/\theta_{01} \approx 100$ they restricted their model to the case $R_1/\theta_{01} \to \infty$. We here extend their model to predict the variations laws with R_1/θ_{01} of both L_{PC1} and the critical ratio r_{uc}. We next validate the extended model by comparing our results with our numerical data.

A. The inner potential core length L_{PC1}

The basic ideas of RVH's model to predict L_{PC1} are the following: the potential core is assumed to be perfectly conical with a basis of radius R_1 and a length L_{PC1}. The entrainment velocity of the fluid within the inner core due to the shear layer on the jet border is assumed to be equal to u_e (see Fig. 18). u_e is assumed to have a constant intensity and to be normal to the side surface of the cone. The mass flux injected in the inner core is equalized with the mass flux crossing the side with the entrainment velocity u_e. For an incompressible fluid, the mass conservation equation can then be written as

$$\frac{\pi {D_1}^2}{4}\overline{u_1} = \frac{\pi D_1}{2}\sqrt{\frac{{D_1}^2}{4} + (L_{\mathrm{PC1}})^2}\,u_e, \tag{13}$$

which leads to

$$\frac{L_{\mathrm{PC1}}}{D_1} = \frac{1}{2}\sqrt{\left(\frac{\overline{u_1}}{u_e}\right)^2 - 1}. \tag{14}$$

Here $\overline{u_1}$ stands for the inner jet bulk velocity. To evaluate the entrainment velocity, RVH used a so-called entrainment hypothesis assuming that the entrainment velocity is proportional to the rms value of the streamwise velocity fluctuation $u'_{x\mathrm{rms}}$ within the shear layer,

$$u_e \approx C u'_{x\mathrm{rms}}, \tag{15}$$

where C is a proportionality constant which depends on the shear flow under consideration. For the coaxial jet, we will determined C through fitting with our numerical results. RVH and Hussain and Zedan[21] experiments showed that the $u'_{x\mathrm{rms}}$ within a mixing layer is given by

$$u'_{x\mathrm{rms}}/U_1 \approx 0.17(r_u - 1). \tag{16}$$

A similar value is found in our numerical simulations (see Fig. 19). Equations (15) and (16) yield the following variation law for the entrainment velocity:

$$u_e/U_1 \approx 0.17C(r_u - 1). \tag{17}$$

For the hyperbolic tangent profile given by Eq. (2), $\overline{u_1}$ is given by

$$\begin{aligned}\frac{\pi {D_1}^2}{4U_1}\overline{u_1} &= \frac{2\pi}{U_1}\int_0^{R_1} U_{\mathrm{med}}(r) r\, dr \\ &= 2\pi\int_0^{R_1}\left[\frac{r_u+1}{2} + \frac{r_u-1}{2}\tanh\left(\frac{r-R_1}{2\theta_{01}}\right)\right] r\, dr.\end{aligned} \tag{18}$$

It gives

$$\frac{\overline{u_1}}{U_1} = \frac{r_u+1}{2} + (r_u-1)B\left(\frac{R_1}{\theta_{01}}\right), \tag{19}$$

with $B(R_1/\theta_{01})$ verifying

$$B\left(\frac{R_1}{\theta_{01}}\right) = \frac{1}{{R_1}^2}\int_0^{R_1} r\tanh\left(\frac{r-R_1}{2\theta_{01}}\right) dr. \tag{20}$$

Equations (14), (17), and (19) provide a new formulation of RVH's model taking into account the variations of L_{PC1}/D_1 with R_1/θ_{01},

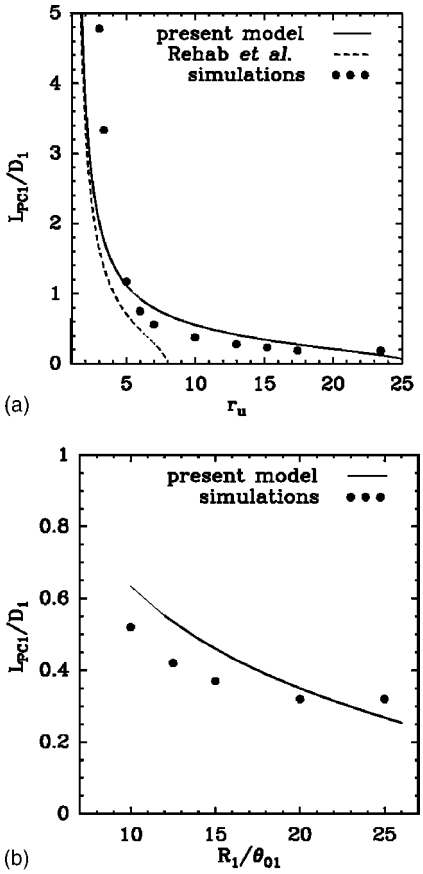

FIG. 20. (a) Evolution with r_u of the inner potential core length L_{PC1} (for $R_1/\theta_{01}=12.5$). (b) Evolution with R_1/θ_{01} of the inner potential core length L_{PC1} (for $r_u=10$). The points represent our simulations, the continuous lines the model given by Eq. (21) and the dashed lines RVH's model [see Eq. (22)].

$$\frac{L_{\mathrm{PC1}}}{D_1} \approx \frac{1}{2}\sqrt{\frac{1}{(0.17C)^2}\left[\frac{1}{2}\frac{r_u+1}{r_u-1}+B\left(\frac{R_1}{\theta_{01}}\right)\right]^2-1}. \qquad (21)$$

Note that original RVH's model is based on a top-hat velocity profile at the inlet with $\overline{u_1} \approx U_1$ which leads to the following expression for L_{PC1} which is independent of R_1/θ_{01}:

$$\frac{L_{\mathrm{PC1}}}{D_1} = \frac{1}{2}\sqrt{\left(\frac{U_1}{u_e}\right)^2-2} \approx \frac{1}{2}\sqrt{\frac{1}{(0.17C)^2}\frac{1}{(r_u-1)^2}-1}. \qquad (22)$$

Figure 20 compares the modified model and RVH's model predictions with the results of our numerical simulations. We found that $C=0.85$ corresponds to the best fit between the theoretical model and the numerical results. As far as the dependence of L_{PC1} with r_u is concerned, the modified model yields a better agreement with the numerical values than the original RVH's model. It reproduces the decrease of the inner potential core length with increasing r_u due to the enhanced turbulence level and the amplified entrainment. The advantage of the modified model lies in its ability to reproduce the correct variations of L_{PC1} with θ_{01} and in particular its decrease when the shear layer becomes steeper.

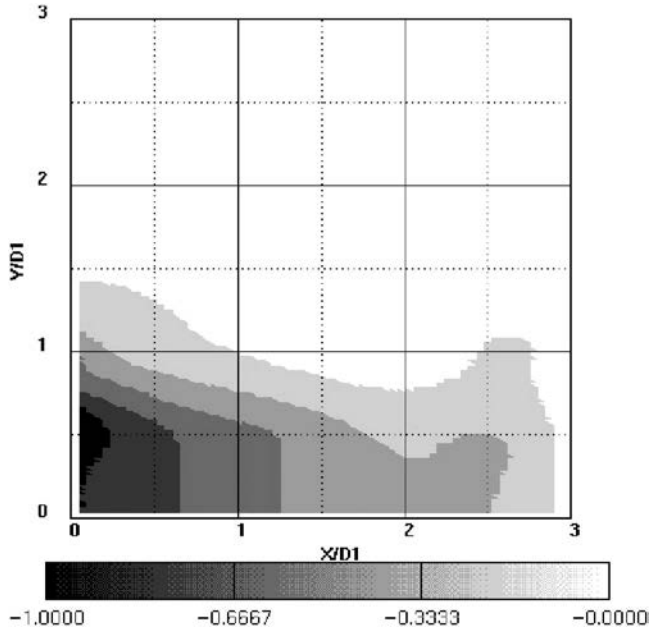

FIG. 21. Normalized mean pressure $(P-P_{\mathrm{ext}})/((1/2)\rho u'^2_{x\mathrm{rms}})$ with P_{ext} reference external pressure plotted in the jet symmetry plane.

B. The critical velocity ratio r_u

The theoretical determination of the critical ratio r_{uc} proposed by RVH is based upon pressure arguments. Due to the curvature of the mean streamlines, the pressure within the inner jet core is lower than the outer pressure. Using phenomenological arguments, Villermaux, Rehab, and Hopfinger[22] estimate this pressure jump ΔP to be of the order of $1/2\rho u'^2_{x\mathrm{rms}}$ with $u'_{x\mathrm{rms}}$ the streamwise rms velocity fluctuation within the external shear layer of the inner core and ρ the fluid density assumed to be constant. Figure 21 shows the isocontours of the mean pressure near the jet inlet for DNS1_13. The pressure is normalized by $1/2\rho u'^2_{x\mathrm{rms}}$ and confirms the above phenomenological arguments. The ambient pressure within the inner core is then of the order of $P_{\mathrm{ext}} - 1/2\rho u'^2_{x\mathrm{rms}}$, where P_{ext} is the reference external pressure. The apparition of a reversed flow is necessarily associated with a stagnation point near the end of the inner potential core. The pressure at this stagnation point will be of the order of $P_S = P_{\mathrm{ext}} - 1/2\rho u'^2_{x\mathrm{rms}} + 1/2\rho \overline{u_1}^2$. If $P_S < P_{\mathrm{ext}}$, a reverse flow takes place and the limiting case therefore corresponds to the balance:

$$1/2\rho u'^2_{x\mathrm{rms}} = 1/2\rho \overline{u_1}^2. \qquad (23)$$

Using the estimation of $u'_{x\mathrm{rms}}$ given by Eq. (16), it yields

$$0.17(r_{uc}-1)U_1 = \overline{u_1}. \qquad (24)$$

Replacing $\overline{u_1}$ by its expression given in Eq. (19), we obtain

$$0.17(r_{uc}-1) = \frac{r_{uc}+1}{2} + (r_{uc}-1)B\left(\frac{R_1}{\theta_{01}}\right), \qquad (25)$$

where $B(R_1/\theta_{01})$ is defined by Eq. (20). Therefore the model to evaluate r_{uc} is

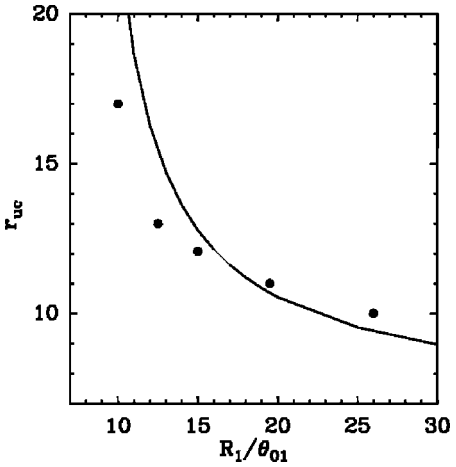

FIG. 22. Evolution with R_1/θ_{01} of the critical velocity ratio r_{uc}. The points represent the numerical simulations and the line the model given by Eq. (26).

$$r_{uc} = \frac{B\left(\frac{R_1}{\theta_{01}}\right) - 0.67}{B\left(\frac{R_1}{\theta_{01}}\right) + 0.33}. \tag{26}$$

Figure 22 shows that the model is able to satisfactorily predict the variation of r_{uc} with R_1/θ_{01} and confirms the importance of this parameter for the limit between the two flow regimes of coaxial jet. Note that the limiting case $R_1/\theta_{01} \to \infty$ leads to $r_{uc} \to 7$: our computations therefore indicate that no backflow region can exist for $r_u < 7$.

V. CONCLUSION

The goal of the present study is to complete previous experimental and numerical works devoted to the study of coaxial jets. The influence of the velocity ratio between the outer jet and the inner jet $r_u = U_2/U_1$ has experimentally been investigated by Rehab *et al.*[6] In these previous studies very small values of the inner and outer jet shear layers thicknesses were considered. However, Rehab *et al.* showed that the shape of the inlet nozzle strongly influences the near jet behavior and the dynamics of the coherent vortices, since different nozzle shapes induce a variation in the steepness of the inner and outer shear layers. Here, we characterize the respective thicknesses of the two shear layers by their momentum thicknesses called θ_{01} and θ_{02}. Even for high Reynolds number jets, a variation of the inner lip thickness of the jet yields a significant variation of θ_{01}. The present paper uses a series of direct numerical simulations to investigate the influence of θ_{01} on the transitional processes in the jet near-field. As shown by Rehab *et al.*, when r_u exceeds a critical value r_{uc}, the jet exhibits a reverse flow region in its inner part called a recirculation bubble. We therefore vary the ratio r_u and the two distinct jet regimes are successively considered: the case without a recirculation bubble ($r_u < r_{uc}$) and with a recirculation bubble ($r_u > r_{uc}$).

We show that, both for $r_u < r_{uc}$ and for $r_u > r_{uc}$, small values of θ_{01} are associated with an earlier jet transition to turbulence due to a faster destabilization of the inner shear layer. We then study in detail the mechanisms responsible for this transition towards a fully developed turbulent state. For $r_u < r_{uc}$, we show that the three dimensionality of the primary jet vortices is greatly enhanced for small θ_{01} and leads to the appearance of secondary streamwise vortices which are stretched between consecutive vortices of the inner and of the outer shear layer. We observe that the transition towards a fully developed turbulent state is strongly linked with the formation and stretching of these streamwise vortices. The critical value r_{uc} separating the regime without and with recirculation bubble is found to be strongly dependent on θ_{01}. For $r_u > r_{uc}$, the shape and the length of the recirculation bubble is seen to be strongly affected by the shape of the inlet profile: the bubble is indeed significantly shortened when θ_{01} is small. The downstream region of the bubble is the siege of intense longitudinal vorticity production yielding the generation of intense streamwise vortices. Again these vortices are associated with a fast flow three-dimensionalization and rapid transition to turbulence.

The thickness of the inner shear layer also affects the evolution of the global quantities such as the jet spreading rate and the length of its two potential cores. For large enough values of r_u, the entrainment by the outer jet leads to an important depletion of the fluid situated near the jet axis. This depletion is associated with a low-pressure region in the jet core and with a curvature of the main velocity streamlines towards the jet axis: this creates a diminution of the jet width corresponding to a pinching phenomenon. This pinching phenomenon is more and more pronounced when θ_{01} decreases. The initial pinching stage is followed by a stage of linear spreading characteristic of a turbulent regime. The linear growth is reached at shorter downstream distances when θ_{01} is small due to the faster turbulence growth within the jet core. The pinching phenomenon is seen to reach a saturation level for $r_u > r_{uc}$.

Rehab *et al.*[6] proposed a theoretical model based on phenomenological arguments to predict the variations of the inner potential core length with r_u. The direct numerical simulations allow to verify that the main assumptions of Rehab's model are justified. This initial model was however limited to an inlet velocity profile with a top-hat shape corresponding with $\theta_{01} \to 0$. We here extend the model to nonzero values of θ_{01} to theoretically predict the variation laws with θ_{01} of the inner potential core length and of the critical ratio r_{uc}. The variation law of the inner potential length with r_u was also determined for finite values of θ_{01}.

The present numerical study allows one to reach a better understanding of the transitional mechanisms leading to turbulence in coaxial jets. This knowledge could be used for control purposes by making possible an efficient manipulation of the flow coherent vortices.

ACKNOWLEDGMENTS

Patrick Begou's help with the numerical-code parallelization is greatly acknowledged. Moreover, numerous discussions with Carlos B. da Silva have contributed to the success of this work. Part of the computations were carried out at the Institut du Développement et des Ressources en Informatique Scientifique (IDRIS, France).

[1]T. J. Williams, M. R. M. H. Ali, and J. S. Anderson, "Noise and flow characteristics of coaxial jets," J. Mech. Eng. Sci. **11**, 133 (1969).
[2]M. Favre-Marinet and E. B. Camano Schettini, "The density field of coaxial jets with large velocity ratio and large density differences," Int. J. Heat Fluid Flow **44**, 1913 (2001).
[3]N. W. M. Ko and W. T. Chan, "The inner regions of annular jets," J. Fluid Mech. **93**, 549 (1979).
[4]H. Rehab, "Structure de l'écoulement et mélange dans le champ proche des jets coaxiaux," Ph.D. thesis, Institut National Polytechnique de Grenoble, 1997.
[5]C. B. da Silva, G. Balarac, and O. Métais, "Transition in high velocity ratio coaxial jets analysed from direct numerical simulations," J. Turbul. **4**, 24 (2003).
[6]H. Rehab, E. Villermaux, and E. J. Hopfinger, "Flow regimes of large-velocity-ratio coaxial jets," J. Fluid Mech. **345**, 357 (1997).
[7]H. Rehab, E. Villermaux, and E. J. Hopfinger, "Geometrical effects on the near-field flow structure of coaxial jets," AIAA J. **36**, 867 (1998).
[8]S. K. Lele, "Compact finite difference schemes with spectral-like resolution," J. Comput. Phys. **103**, 16 (1992).
[9]C. Canuto, M. Y. Hussaini, A. Quarteroni, and T. A. Zang, *Spectral Methods in Fluid Dynamics* (Springer, New York, 1987).
[10]M. A. Gonze, "Simulation numérique des sillages en transition à la turbulence," Ph.D. thesis, Institut National Polytechnique de Grenoble, 1993.
[11]C. B. da Silva and O. Métais, "Vortex control of bifurcating jets: a numerical study," Phys. Fluids **14**, 3798 (2002).
[12]C. B. da Silva and O. Métais, "On the influence of coherent structures upon interscale interactions in turbulent plane jets," J. Fluid Mech. **473**, 103 (2002).
[13]C. B. da Silva, "The role of coherent structures in the control and interscale interactions of round, plane and coaxial jets," Ph.D. thesis, Institut National Polytechnique de Grenoble, 2001.
[14]H. A. Warda, S. Z. Kassab, K. A. Elshorbagy, and E. A. Elsaadawy, "An experimental investigation of the near-field region of a free turbulent coaxial jet using LDA," Flow Meas. Instrum. **10**, 15 (1999).
[15]G. Buresti, P. Petagna, and A. Talamelli, "Experimental investigation on the turbulent near-field of coaxial jets," Exp. Therm. Fluid Sci. **17**, 18 (1998).
[16]N. W. M. Ko and A. S. H. Kwan, "The initial region of subsonic coaxial jets," J. Fluid Mech. **73**, 305 (1976).
[17]J. C. R. Hunt, A. A. Wray, and P. Moin, "Eddies, stream, and convergence zones in turbulent flows," Annual research briefs, Center for Turbulence Research, Stanford, 1988.
[18]Y. Dubief and F. Delcayre, "On coherent vortex identification in turbulence," J. Turbul. **1**, 11 (2000).
[19]O. Métais, "Large-eddy simulations of turbulence," in *New Trends in Turbulence*, edited by M. Lesieur *et al.* (Springer, New York, 2001), pp. 113–186.
[20]G. Balarac and O. Métais, "Coherent vortices in coaxial jets," in *Advances in Turbulence X*, edited by H. I. Anderson and P.-Å. Krogstad (CIMNE, Barcelona, 2004), pp. 149-152.
[21]A. K. M. F. Hussain and M. F. Zedan, "Effects of the initial conditions on the axisymetric free shear layer: effects of the initial momentum thickness," Phys. Fluids **21**, 1100 (1978).
[22]E. Villermaux, H. Rehab, and E. J. Hopfinger, "Breakup regimes and self-sustained pulsations in coaxial jets," Meccanica **29**, 393 (1994).